CAMBRIDGE
UNIVERSITY PRESS

Article

Morphological features of halloysite nanotubes as revealed by various microscopies

Nia Gray-Wannell[1,2], Pablo Cubillas[3], Zabeada Aslam[4] (iD), Peter J. Holliman[2] (iD), H. Christopher Greenwell[3] (iD),
Rik Brydson[4] (iD), Evelyne Delbos[1], Laura-Jane Strachan[1], Martin Fuller[5] and Stephen Hillier[1,6] (iD)

[1]The James Hutton Institute, Craigiebuckler, Aberdeen, UK; [2]Chemical Engineering Materials Environment Group, Swansea University, Bay Campus, Swansea, UK; [3]Department of Earth Sciences, Durham University, Durham, UK; [4]School of Chemical and Process Engineering, University of Leeds, Leeds, UK; [5]Centre for Plant Science, School of Biology, University of Leeds, Leeds, UK and [6]Department of Soil and Environment, Swedish University of Agricultural Sciences, Uppsala, Sweden

Abstract

Nine halloysite nanotubes (HNTs) have been examined using scanning electron microscopy (SEM), atomic force microscopy (AFM) and (cross-sectional) transmission electron microscopy (TEM) to evaluate details of their external and internal morphologies. The samples span morphologies within the cylindrical to prismatic-polygonal framework proposed by Hillier *et al.* (2016). The 'carpet roll' model assumed in the conceptualization of most technological applications of HNTs is shown to be far too simplistic. Both cylindrical and prismatic forms have abundant edge steps traversing their surfaces that, by analogy with plates of kaolinite, correspond to prism faces. The mean value for the diameter of the central lumen of the tubes is 12 nm. Numerous slit-like nanopores, with diameters up to 18 nm, also occur between packets of layers, particularly in prismatic forms at the junction between a central cylindrical core and outer packets of planar layers. These pores expose aluminol and siloxane surfaces, but unlike the lumen, which is assumed only to expose an aluminol surface, they do not extend along the entire length of the nanotube. Edge steps seen most clearly by AFM correspond in height to the packets of layers seen in TEM. TEM cross-sections suggest that tube growth occurs by accretion of a spiralled thickening wedge of layers evolving from cylindrical to polygonal form and reveal that planar sectors may be joined by either abrupt angular junctions or by short sections of curved layers. A more realistic model of the internal and external morphologies of HNTs is proposed to assist with understanding of the behaviour of HNTs in technological applications.

Halloysite nanotube (HNT) clay minerals ($Al_2SiO_2(OH)_4.nH_2O$) are found in abundance in many rocks and soils worldwide (Joussein *et al.*, 2005). HNTs are differentiated structurally from their kaolin subgroup relatives, namely kaolinite, dickite and nacrite, by a naturally occurring interlayer of water molecules (Santagata & Johnston, 2022). The presence of this water layer gives halloysite a 10 Å layer spacing, but the water layer is readily and irreversibly lost to produce the more commonly observed dehydrated 7 Å form. Halloysite also occurs in a variety of morphologies: platy, spheroidal and tubular, with the most common being the tubular form (Joussein *et al.*, 2005). Even though morphology is not a defining feature of a mineral, the predominance of this tubular morphology in halloysite compared to the platy morphology of kaolinite is, in essence, another distinguishing feature of halloysite. The curved layers of the halloysite tubular form probably reflect the basic requirement to correct the lateral misfit between the smaller octahedral and larger tetrahedral sheets of the fundamental kaolin 1:1 layer (Bates *et al.*, 1950), with rolling of the layers being one of several ways to alleviate this misfit. Concerning tubular halloysites, two distinct morphologies have been identified: cylindrical and prismatic-polygonal. Nanotubes of cylindrical morphology have a circular or ovoid cross-section and are typically smaller in length and diameter than prismatic-polygonal forms (Hillier *et al.*, 2016), which have planar external surfaces reflecting an internal arrangement of 'sectors' (Chukhrov & Zvyagin, 1966; Kogure *et al.*, 2013).

Due to their nanotube shape, high aspect ratio, natural abundance and low toxicity, technological interest in halloysite has increased enormously in recent years (Churchman *et al.*, 2016), and they have been applied in a wide variety of industries, fulfilling various functions in drug-delivery systems (Lvov *et al.*, 2016; Massaro *et al.*, 2017), polymer nanocomposites (Du *et al.*, 2008; Pasbakhsh *et al.*, 2013), historical site restoration (Cavallaro *et al.*, 2020) and lithium sulfur batteries (Lin *et al.*, 2017), with ever-increasing additional applications. Fundamentally, the use of halloysites in these technologies relies on an understanding of their surface chemistry and surface reaction sites. This is in terms of both the behaviour of these sites as well as the distribution of different sites in relation to the details of nanotube

morphology. Additionally, this understanding has implications for their potential to be functionalized in various application-specific ways.

In many, if not most, of the suggested technological applications, a rather simplistic morphological model of HNTs is presented or implied. Typically, this is one of a smooth outer siloxane surface with minimal external surface edge sites, an inner aluminol surface to the so-called central 'lumen' (i.e. the hollow core of the tube) and pH-dependent tube terminus silanol and aluminol group edge sites. The following publications are illustrative (Yuan *et al.*, 2015; Kim *et al.*, 2017, Gkouma *et al.*, 2021; Grylewicz & Mozia, 2021), but thousands of recent publications that assume this model could be cited. Although this simplistic model of halloysite (schematic shown as in Fig. 1) has been assumed in a multitude of studies, especially in relation to technological applications, there is rare acknowledgement that the outer surface of the HNT should not simply be considered as a smooth continuous siloxane surface but, in reality, will be more complex. For example, authors such as Yuan *et al.* (2008) observed defects on the surface of halloysite using atomic force microscopy (AFM) and noted that these could account for extra surface hydroxyl sites available for reaction. Additionally, it has been known for some time that the central lumen is not necessarily the only type of nano-confined pore space present in halloysite with tubular morphology (Churchman *et al.*, 1995) and that additional pores may occur as gaps and separations between the rolled layers.

Imaging techniques such as scanning electron microscopy (SEM), transmission electron microscopy (TEM) and AFM can be used to analyse various features of the surface and internal structure of tubular halloysites and to differentiate between their distinct morphologies. However, problems can be encountered when attempting to take high-resolution images of halloysite samples due to issues such as their beam sensitivity (Kogure *et al.*, 2011) and small size. Several authors have studied halloysites using some or all of the above microscopy techniques (e.g. Bates & Comer, 1957; Dixon & McKee, 1974; Kohyama *et al.*, 1978; Kogure *et al.*, 2011, 2013).

The aim of the present study was to use SEM, AFM and TEM imaging on the same suite of samples to provide some additional observations upon which to base an improved conceptual model of the real internal and external morphological features of HNTs. The observations were made within the framework of the cylindrical–prismatic-polygonal scheme of the physical and mineralogical properties of HNTs, as proposed by Hillier *et al.* (2016) and elaborated on by Drits *et al.* (2018).

Materials

Nine samples of HNTs originating from a variety of localities in the USA, China, Türkiye, and Scotland were studied (Table 1). The mineralogical and physical properties of six of these samples are documented in Hillier *et al.* (2016), including purity as estimated using X-ray powder diffraction methods. The halloysite contents of three additional samples (22US, 23US and 24US), all from the USA, were determined specifically for the present study. Samples were selected to cover a range of dominant prismatic-polygonal *vs* dominant cylindrical morphologies, and some are obvious mixtures of the two morphological types. Cylindrical forms have the highest specific surface areas, whereas the best developed prismatic-polygonal forms have the lowest. Specific surface area is correlated with the so-called Cylindrical/Prismatic 'CP' index as measured from the characteristics of the (20,13) X-ray diffraction band (Hillier *et al.*, 2016). Hereafter, the two different types will simply be referred to as 'cylindrical' and 'prismatic'. All samples are largely dehydrated and therefore in the so-called 7 Å form. X-ray diffraction patterns of all nine samples are shown in Fig. S1, deposited as supplementary material.

Methods

Scanning electron microscopy

Samples were prepared for SEM analysis using one of two methods. For those samples available as intact pieces, the first method involved drying of the sample in an oven at 105°C for several days
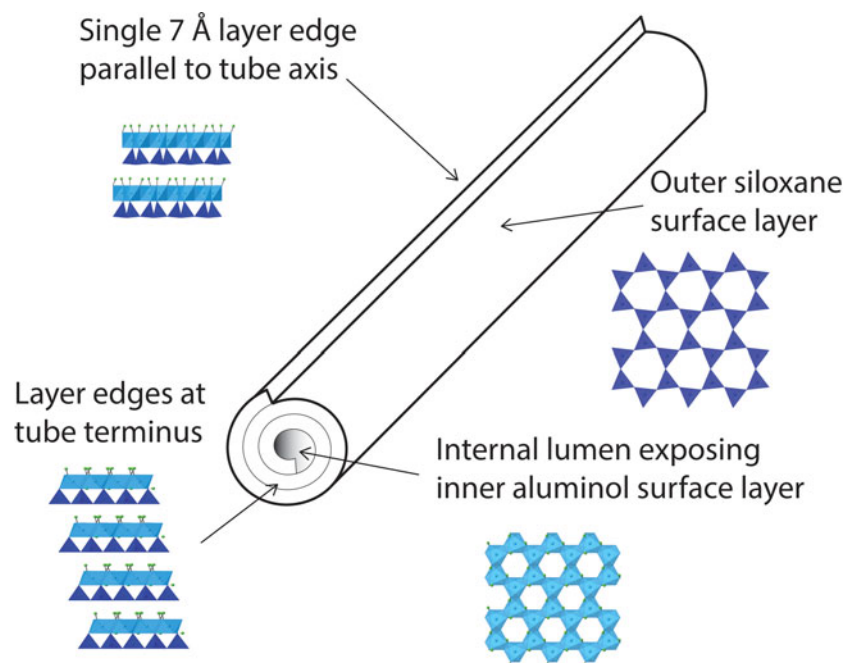

Figure 1. Simple 'carpet roll' morphological model of HNTs formed as a spiralled 7 Å (1:1 kaolin layer) as currently assumed in most technological applications. The kaolin layer is composed of octahedral (light blue) and tetrahedral (dark blue) sheets as illustrated by the polyhedral models. The layering depicts a single 7 Å kaolin layer.

Table 1. HNT sample details.

Sample ID	Location	Dominant morphology	Halloysite (wt.%)	SA (m^2 g^{-1})	'CP' index
4Ch[a]	Defang, China	Cylindrical	98.5	80	0.354
5Ch[a]	Bifa, China	Cylindrical	99.8	69	0.326
11Sc[a]	Elgin, Scotland	Prismatic	99.4	16	0.083
12Tu[a]	Türkiye	Cylindrical	88.0	61	0.339
17US[a]	Dragon Mine, USA	Prismatic	99.0	30	0.213
21US[a]	Bovill Deposit, USA	Prismatic	93.5	28	0.172
22US	Wagon Wheel Gap, USA	Prismatic	98.0	26	0.149
23US	Dragon Mine, USA	Prismatic/cylindrical	86.9	59	0.247
24US	Dragon Mine, USA	Prismatic/cylindrical	98.1	49	0.264

[a]Data from Hillier *et al.* (2016).
SA = specific surface area (determined using N$_2$ adsorption and the Brunauer–Emmett–Teller (BET) equation).

then breaking to expose a fresh fracture surface that was platinum coated before analysis. The second method involved initial gentle crushing and homogenization of the intact or powdered sample, ~10 mg of which was weighed into a beaker to which 100 ml of deionized water was added along with two drops of Calgon to aid dispersion. The suspension was sonicated for 5 min to ensure even dispersion and a single drop immediately deposited on a silicon wafer supporting a 3 mm nickel grid. The grid ensured that the droplet dried to produce a more even distribution of particles across the surface of the silicon wafer. Once dry, the samples were platinum coated to reduce charging. SEM images for both types of sample preparation were taken using a Carl Zeiss Sigma VP field emission scanning electron microscope (FEG-SEM), operated between 10 and 20 kV.

Atomic force microscopy

Samples were prepared for AFM by dispersion of the halloysite in deionized water and pipetting onto a mica surface, which was placed into an oven to dry. AFM images were acquired using a Multimode AFM, Nanoscope V, Multimode 8, which operates at a frequency of ~2 Hz. The instrument was operated in PeakForce™ scanning mode, which allows extreme tip-to-sample force control, making it ideal for small crystals and soft samples as it minimizes any direct tip–sample interaction (i.e. it reduces the chances of the sample being moved or disturbed by the tip). Bruker Scanasyst-air probes, with a spring constant of 0.4 N m^{-1} and a nominal tip radius of 2 nm were utilized. Analysis of the AFM images was conducted using *ImageJ* (Rueden *et al.*, 2017), *JPK SPM Data Processing Analyser* version 6.1.79 and *NanoScope Analysis* 1.5.

Cross-sectional analysis by transmission electron microscopy

Samples representative of both cylindrical and prismatic HNTs were embedded in TAAB Lemix L029 resin for cross-sectional analysis by TEM. Approximately 50 mg of sample was mixed with 2.5 mL of Lemix A, and the samples were gently sonicated. The dispersion was then mixed with 5.5 mL Lemix B, 0.2 mL Lemix C and 2 mL Lemix D, and the material was thoroughly shaken and gently sonicated. The samples were hand shaken and syringed into modified pipette tips that had an area cut out to allow for air contact before being cured overnight at 70°C in an oven. The cured resin samples were prepared as sections for analysis by TEM using microtome sectioning. TEM analysis was conducted on a FEI: Titan Themis instrument operated at an accelerating voltage of 300 kV. Halloysites are highly beam

sensitive, and so a beam current of 0.5 nA was used throughout to help reduce beam damage. Measurements on the TEM images were conducted using *ImageJ* (Rueden *et al.*, 2017).

Results

By way of introduction to the microscopy results, within the vacuum environment of the SEM and TEM the HNTs will naturally dehydrate, reducing any existing (hydrated) 10 Å interlayer spacings to (dehydrated) 7 Å spacings. In general, we assume no change in morphology or surface features as a result of any such dehydration. Additionally, many of the samples we have analysed have been exposed to ambient laboratory conditions for an extended time (months to years), which typically means that they will already have been in predominantly 7 Å form prior to examination by the various microscopies, as no special handling was employed to attempt to preserve the primary 10 Å forms.

Scanning electron microscopy

A simple comparison of the two morphological types – cylindrical and prismatic – is shown by the collection of SEM images in Fig. 2. Distinction between the two morphological types in terms of particle size, shape, form and features is readily made. Thus, the cylindrical examples (Fig. 2a–c) are clearly of smaller diameter than the prismatic forms, and their outer surfaces appear continuously curved, with circular or oval tube ends.

By contrast, the outer surface of the prismatic particles (Fig. 2d–f) appears divided into a series of flat faces. The faces meet at well-defined angles, forming obvious linear intersections, which, together with the faces, are arranged parallel to the long axis of the tubes, thus defining their prismatic form. In the prismatic forms, most of the linear edges where faces intersect appear to represent an abrupt kinking or bending of a contiguous surface. For the prismatic examples, it is not easy to ascertain the total number of flat faces using SEM because typically not all sides are visible together. However, for the samples examined as intact specimens where complete circumferences can be seen, some appear as five-sided polygons (Fig. 2f). Additionally, for most other particles of prismatic type, the restricted number of sides that are visible in SEM images and their arrangement on the part of the tube that can be seen suggest that the total number of faces is also limited to a similar small number. Another type of edge, defined by a clear step in height, along with a more irregular, angular path along the surface of the particles (e.g. Fig. 2d), defines various layer terminations (hereafter 'step
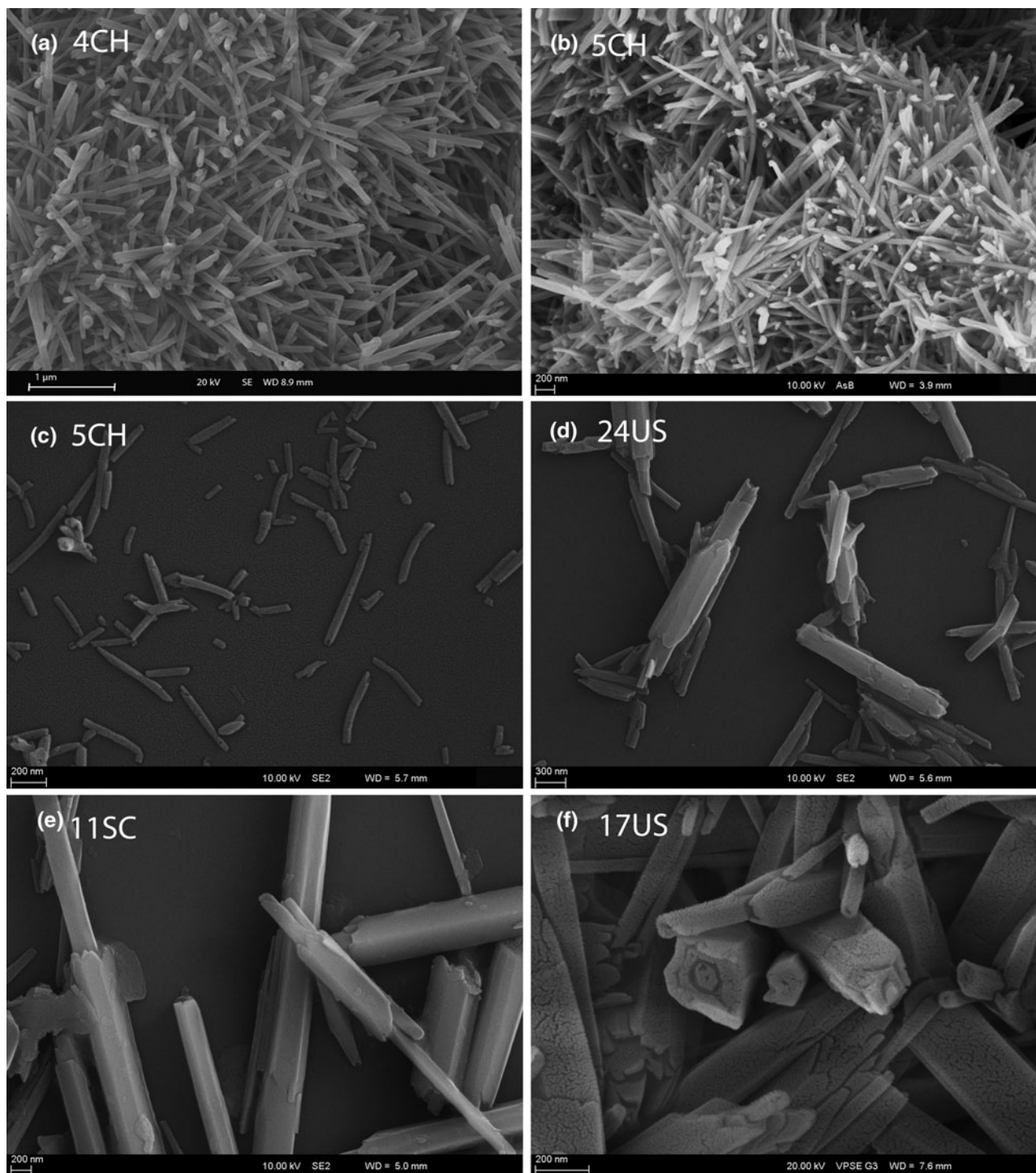
Figure 2. SEM images of small cylindrical and larger prismatic HNTs. For sample IDs, refer to Table 1.

edges') arranged along the lengths of the tubes. Additionally, spindle-like particles are common in many samples (e.g. Fig. 2d–f), where the thicker parts of the tubes are the shortest parts and a thinner portion of the tube protrudes from one or both ends. In many cases, this change in tube thickness appears to occur in several 'telescopic' steps down to successively thinner inner tubular forms. Furthermore, examination of the ends of the telescopic sections corresponding to the thicker parts of the tubes often shows termination in a half pseudo-hexagonal form, such that the terminal edge face is normal to the axis of the tube

(Fig. 2d,e). Finally, as can also be seen in many of the images in Fig. 2, although each sample may be predominantly either cylindrical or predominantly prismatic, the samples are not homogeneous populations of morphological types, and the reality for most is some mixture of the two distinct morphologies.

Atomic force microscopy

In agreement with the SEM images, prismatic samples (Fig. 3d–f) in AFM display rectangular flat faces along the axis of the
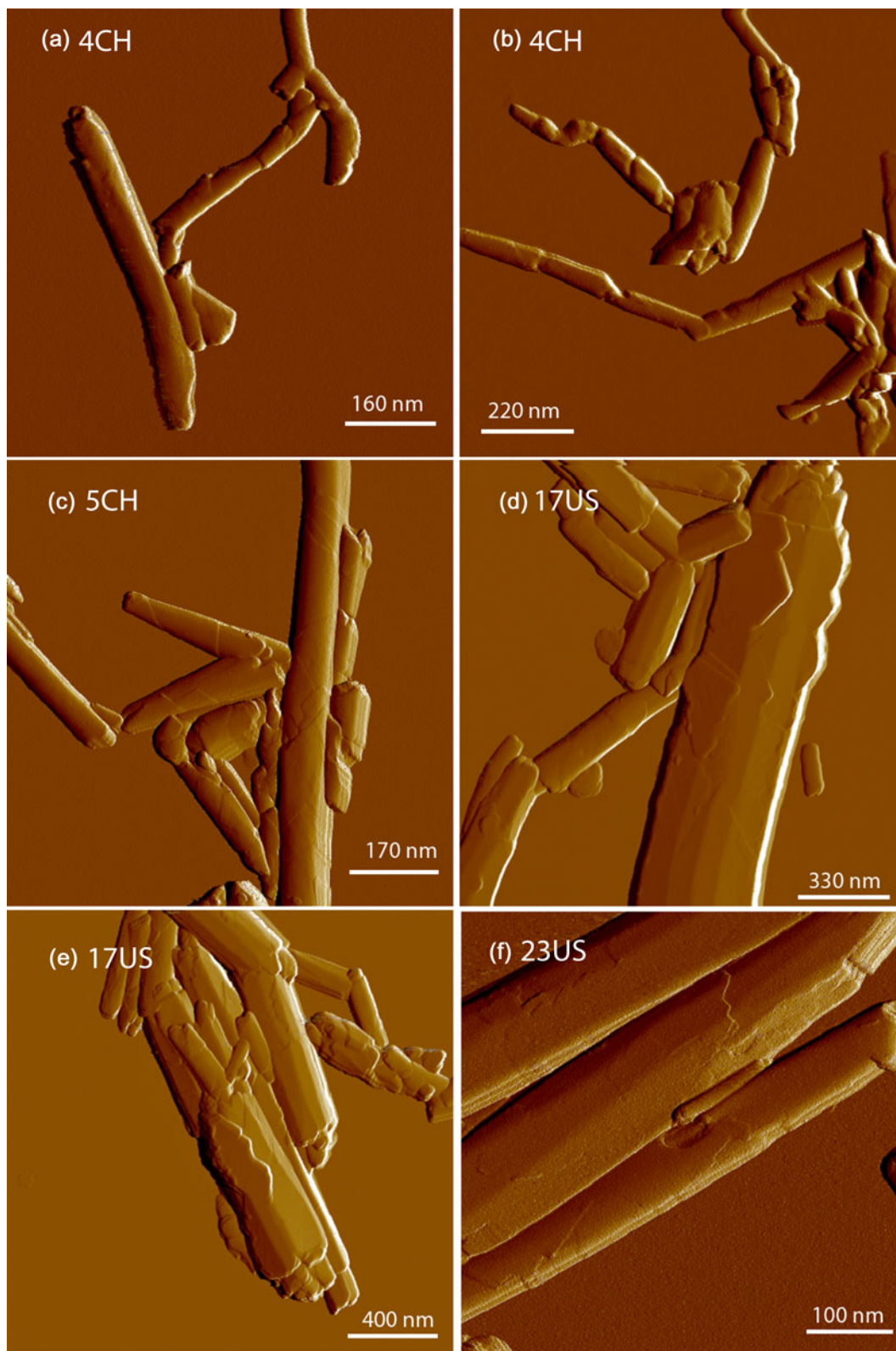
Figure 3. AFM peak force error images of HNTs. For sample IDs, refer to Table 1.

nanotubes with well-defined boundaries between adjacent flat faces. Indeed, AFM images provide the clearest illustrations of the prismatic morphology. The additional edges traversing along the length of the tubes that are associated with a step change in the height of the tube surface are also more readily apparent in the AFM images. These step edges are not singularly linear in form, and the AFM images reveal that many have an obvious 'saw tooth' arrangement. Attempts to measure the angles between
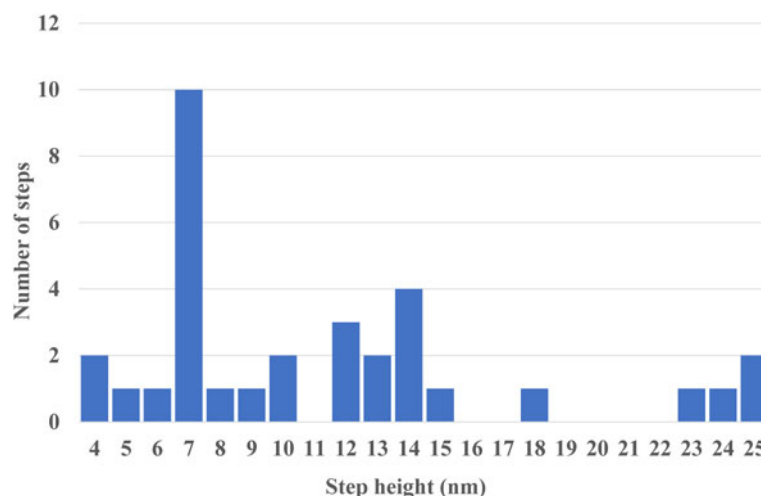
Figure 4. Histogram of measured edge step sizes on the surface of HNTs (height in nanometres) from AFM images of three different prismatic samples. Total number of steps measured = 33.

adjacent 'teeth' indicate values close to 120°. Furthermore, these edges and the angles along them also show a regular arrangement with respect to the tube axes, indicating that they are consistently orientated in relation to the underlying symmetry of the halloysite crystal structure (Fig. 3d,e). Generally, these 'saw tooth' terminations on different faces are arranged pointing in the same direction around the tube; however, occasional examples were noted where 'teeth' can be found pointing in opposite directions on a given tube.

Attempts to measure the heights of the steps from the AFM images on a variety of prismatic examples showed them to range from 4.2 to 24.9 nm, with clustering at ~7 nm and 12–14 nm (Fig. 4). Additionally, measurements of five rectangular areas on one prismatic sample (17US) gave an average ratio of edge length to the area over which the edges were distributed of 0.0083 ± 0.0036.

In addition to the edge steps on the surface of the HNTs observed with AFM, the ends of the prismatic tubes often display a staggered and stepped shortening (e.g. Fig. 3e) with respect to the arrangement of successive layers (or packets of layers – see below). Sometimes this extension is extreme, creating the spindle-like structures, as seen most readily in the SEM images, but AFM also shows that there is often a gradual progression, such that the ends of the tubes show a closely spaced 'staircase' arrangement of steps up to progressively shorter sections of the tube. At these ends, as was indicated in SEM images, the edge terminations are orientated normal to the tube axis (Fig. 3d,e), which, again, as with the consistent orientation of the 'saw tooth' edge steps along the faces of the tube, indicates an underlying control over their arrangement by the halloysite crystal structure and its orientation with respect to the long axis of the nanotubes. Due to the orientation of the samples in AFM, it was not possible to count the total number of sides of prismatic samples, but the number of flat faces visible is in some cases suggestive of there being more than the approximately five or so sides that appeared to be common in the SEM images.

Clear AFM images of the cylindrical HNTs were much more difficult to obtain, primarily due to their much smaller size, which often resulted in the samples moving around during analysis. Nevertheless, edge steps are still clearly visible on the surface of the cylindrical nanotubes (Fig. 3a–c), with those that were measured indicating step heights of ~7 nm (*n* = 3). It was also noted that the edge steps typically traverse the surface of the nanotubes

at acute angles to the axis of the tube. Angle measurements suggest clusters near ±30° and ±60° with respect to an arbitrarily selected positive direction for the tube axis. However, other angles are also apparent – for example, where the tube form is distorted towards that of a cone in some of the tubes shown in Fig. 3c. As with the prismatic nanotubes, edges or steps parallel to the tube axis, as depicted in the schematic of Fig. 1, were not apparent. Although samples 4Ch and 5Ch shown in Fig. 3a–c are predominantly cylindrical samples, larger prismatic nanotubes were also noted in these samples, indicating that, as with the SEM observations, even though a sample may be dominated by one morphology, examples of the other morphology are typically present amongst the population of tubes.

Transmission electron microscopy

TEM analysis of the microtome cross-sections of a range of prismatic and cylindrical halloysites resulted in the successful acquisition of many useful images, some of which are illustrated in Fig. 5 (cylindrical) and Fig. 6 (prismatic). As with both SEM and AFM analyses, it was clear that although a given sample might be considered as predominantly cylindrical or prismatic in morphology, all samples contained examples of the other morphology.

TEM cross-sectional images of the cylindrical halloysites (Fig. 5) appear to indicate a simple structure with continuous and seemingly even layer (1:1) spacing, with no obvious segregation into packets of layers by intervening pores. Where it could be assessed, in all cases the tubes appear to be constructed of layers arranged in a spiral rather than in a concentric manner. However, further addition of layers to the central part of the cylinders seems often to emanate from a point by addition of a thickening wedge of successive spiralling layers (e.g. Fig. 5a,e).

Most cross-sections from the prismatic samples also show clear evidence of a cylindrical core at the centre of the nanotube (Fig. 6), and in both types of nanotube measurements of the diameter of the central lumen show very similar sizes, with an average of 12.1 nm (standard deviation = 4.1, *n* = 24) for the prismatic samples compared to 12.3 nm (standard deviation = 2.7, *n* = 25) for the cylindrical ones. Both types also show similar ranges of diameter measurements for the central lumen, varying from 7.5 to 24.1 nm for prismatic and from 8.0 to 18.7 nm for cylindrical examples.
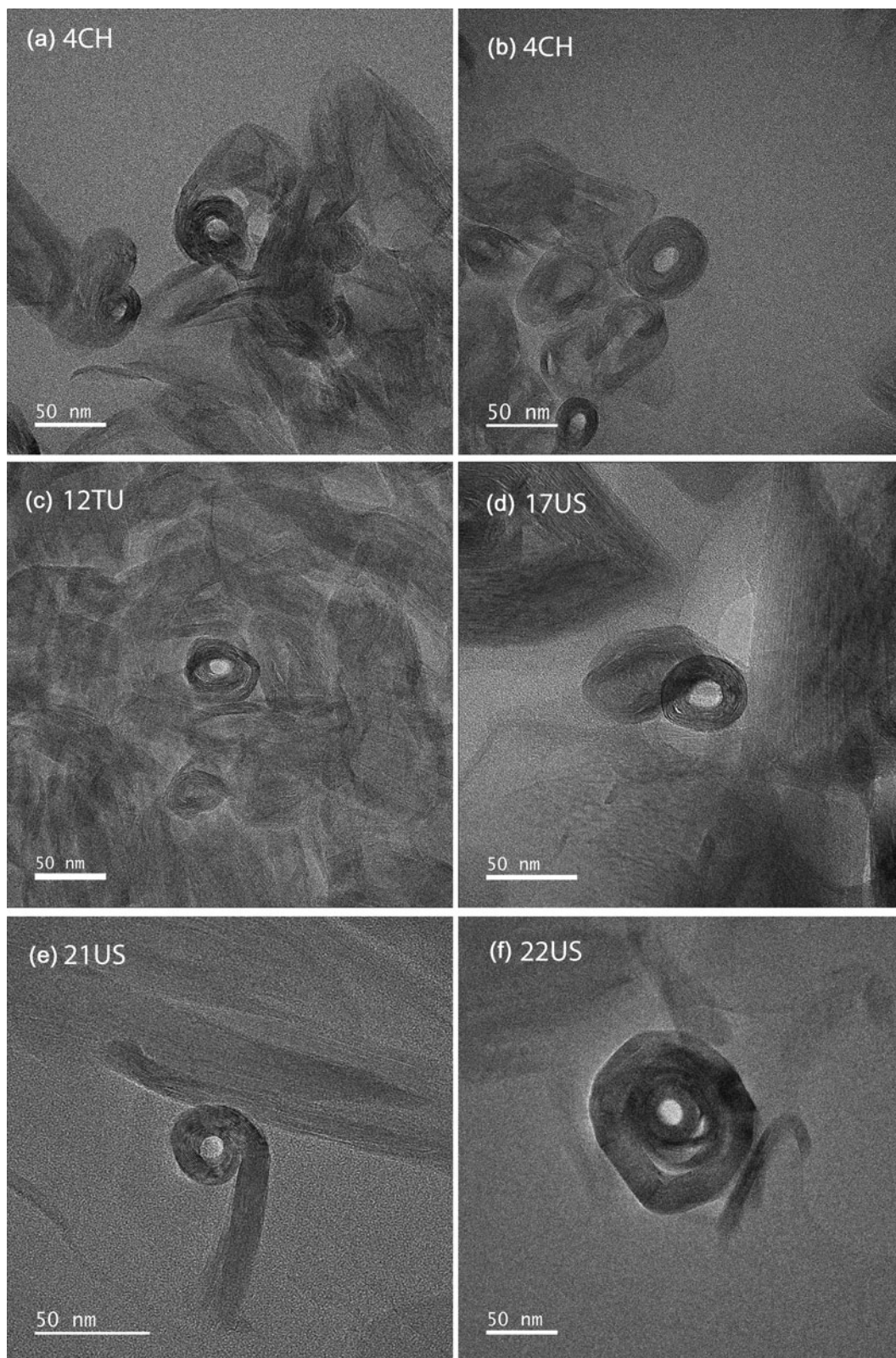
Figure 5. TEM images of the cross-sections of a variety of cylindrical HNTs. For sample IDs, refer to Table 1.

Another feature shown by the cross-sections of the prismatic forms are the clearly defined, polygonal linear outlines of their flat external faces, along with frequent, often very thin linear junction zones that extend radially from the interior in straight lines towards the external corners of the polygonal cross-sections. However, in addition to these abrupt junctions, there are also many examples where sectors of flat layers in the prismatic samples are joined by short sections of curved layers (Fig. 6c,e).
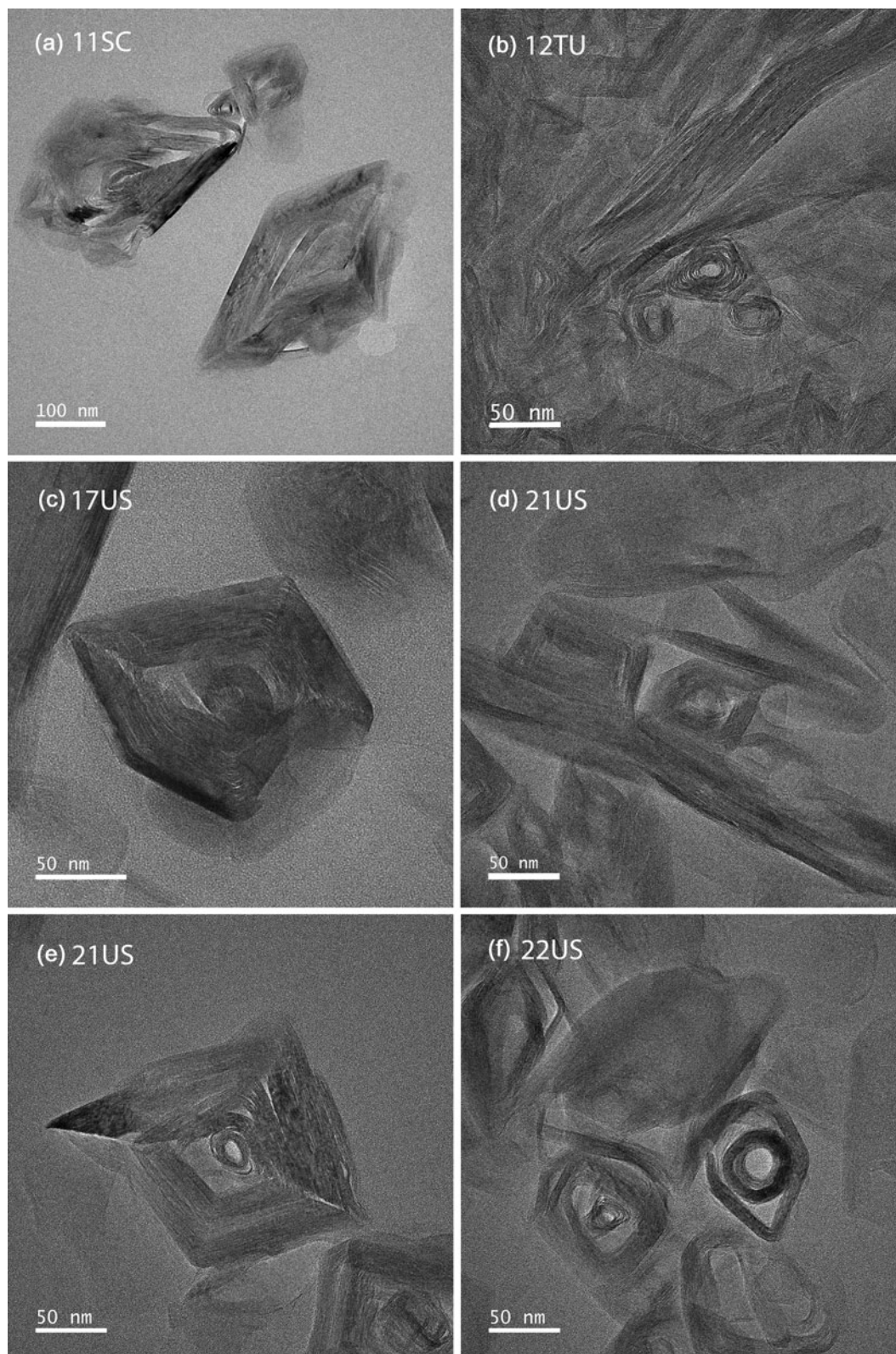
Figure 6. TEM images of the cross-sections of a variety of prismatic HNTs. For sample IDs, refer to Table 1.

Counting the number of external faces on the prismatic forms indicated that out of 45 individual nanotubes counted, 30 had 5 sides, 13 had 4 sides and (because the distinction between some sides was unclear) 2 were judged to have between 4 and 5 sides.

Difficulty distinguishing some sides may be the result of mechanical distortion during sectioning. Additionally, the angles of intersection between sides were measured and range from an acute 57° to an obtuse 159°, with a mean of 117° and a mode of 122°.

Another essentially ubiquitous feature of the prismatic examples is a division in cross-section images into packets of (1:1) layers separated by slit- or triangular-shaped pores, with up to four such layer packets observed in some samples. Analysis of 17 prismatic HNTs across the range of samples shows that the average total number of layers in prismatic samples is 39 (Table 2), with the average number of layers in individual layer packets ranging from 12 to 41. There is also a large variability in the size of the prismatic halloysites, which displayed an average diameter of 135.2 nm ($n = 25$), the largest measured having a diameter of 420.3 nm and the smallest having a diameter of 43.6 nm. By contrast, the cylindrical nanotubes had an average diameter of 57.5 nm ($n = 26$). The data in Table 2 reflect a general trend for layer packet thickness to increase with increasing HNT diameter.

Measurements of the pores that occur between the packets in prismatic examples indicated a wide range of lengths between 0.88 and 18.1 nm, with an average width of 4.5 nm ($n = 15$). Overall, these pores occur most commonly at the boundary that marks a change from an inner cylindrical core of curved layers to a succeeding packet of planar layers. Two of the prismatic tubes had outlying largest pore diameters of 16.8 and 18.1 nm, respectively, highlighting the large variation in pore size that may occur. However, it is also important to point out that where prismatic tubes were seen in section along their length (e.g. Fig. 6b), it is apparent that the slit-like pores do not run along the entire length of the tube. In summary, cross-sectional TEM analysis revealed the occurrence of pores in all of the prismatic samples, which suggests that they are a common feature in the prismatic morphology of HNTs.

Discussion

The present study has focused on the analysis of the morphological features of a series of HNT samples using three complimentary microscopies, namely SEM, AFM and TEM. Analysis was framed in the context of the dominant type of HNT morphological form in the different samples (i.e. cylindrical *vs* prismatic), and the primary question driving the study was the validity of the simplistic morphological model of HNTs that is used as the basis of the conceptualization and design of many technological applications of HNTs.

Images from all three microscopies revealed that although a sample may be classified as predominately either prismatic or cylindrical, at an individual level the particles in any given sample are not exclusively of one morphological type, and examples of prismatic forms can be found in predominantly cylindrical samples and vice versa. This is not surprising given that the intermediate values of characteristics such as specific surface area and

'CP index' (Table 1) of some samples indicate that they should be composed of a mixture of prismatic and cylindrical forms (Hillier *et al.*, 2016), but it is nonetheless useful to note that diversity of form can be readily observed with the various microscopies, even in samples that are close to the poles of the morphological types. The simple division into predominant nanotube type is reflected in major differences in nanotube size as evidenced directly in the illustrated examples for each of the three microscopies (Figs 2, 3, 5 & 6) and most clearly in the present investigation by the TEM cross-sectional images (Figs 5 & 6).

Analysis of the TEM cross-sections confirms that cylindrical nanotubes are of much smaller diameter compared to prismatic types. This finding was also emphasized in Hillier *et al.* (2016) based on measurements made using image analysis methods of tube diameters in SEM images. However, despite the large differences in external diameter between the two morphologies, direct measurements of the diameter of the central lumen in the TEM cross-sections indicate an essentially identical lumen size for both types at 12.1 nm (standard deviation = 4.1, $n = 24$) for the prismatic samples as compared to 12.3 nm (standard deviation = 2.7, $n = 25$) for the cylindrical examples. These diameters are in the same range as the average lumen diameters of 13.5 nm measured by differential pore-volume plots by Hillier *et al.* (2016) for a range of cylindrical and prismatic HNTs. In both forms the central lumens are also similarly circular or oval in cross-section. However, oval shapes may well reflect examples where the tube cross-sections are aligned obliquely to the axis of the tubes, as there is no guarantee that the sections observed were cut normal to the tube axis and no attempt was made to try to determine whether this were the case, such as from TEM lattice fringes or diffraction contrasts. The TEM images also revealed that the cylindrical samples are most frequently composed of a single coherent packet of layers averaging some 15 (1:1 unit) layers thick. This corresponds well to the 10–15 layers often quoted in the literature with reference to cylindrical HNTs (e.g. Lvov *et al.*, 2016). However, the polygonal cross-sections of prismatic forms are more complex, often divided by pores of various shapes and sizes into up to four distinct packets of layers averaging 12–41 (1:1 unit) layers thick. This is a feature that was also observed in the early pioneering study by Dixon & McKee (1974), who noted up to six packets with intervening layer separations within a single particle.

Perhaps the most significant observation from the cross-sectional TEM images of the present study is that most prismatic samples also contain a central core that is cylindrical in form. Presumably, this feature is also reflected in the SEM images of the spindle-like particles observed most readily in samples prepared as dispersions, wherein the smallest tube diameter, often protruding in a telescopic-arranged succession of tubes from

Table 2. Layer measurements taken from TEM cross-sections.

Tubular morphology	Layer position	*n*	Average number of layers	Standard deviation
Cylindrical	All	15	15	3.8
Prismatic	Average total layers	17	39	23.2
Prismatic	Innermost layer packet	17	12	3.9
Prismatic	First successive layer packet	14	19	10.1
Prismatic	Second successive layer packet	6	19	4.2
Prismatic	Third successive outer layer packet	2	41	8.0

Note: Layer packets are defined as distinct segments of the HNT separated by a change in morphology/slit-like pores or voids in the structure. The innermost packet of layers in the prismatic samples corresponds to the central core of the HNT cross-sections.

shorter and much thicker prismatic parts, exhibits the curved surface of a cylindrical form of tube. Occasionally, cylindrical cores are also indicated in the morphologies of tube ends seen in fracture surface SEM images (Fig. 2f), although such details are easily obscured by the application of coatings applied to reduce charging in such specimens. The TEM cross-sections, however, represent the clearest evidence that a central cylindrical core, with dimensions that match 'free' cylindrical HNTs, is a common feature in the larger prismatic forms.

This observation is an important one in relation to any debate about the origin of prismatic forms of HNTs. In this context, Kogure *et al.* (2013) suggested that polygonal prismatic forms of HNTs may be a result of dehydration of an original cylindrical form. However, Hillier *et al.* (2016) later speculated that the larger size of prismatic forms suggested that they were the result of a change from cylindrical to planar growth, with this change occurring as HNTs increased in size, eventually to beyond the point where layer curvature was an energetically favourable way to accommodate the fundamental misfit between tetrahedral and octahedral sheets in the 1:1 kaolin unit layer. The TEM cross-sections provide direct evidence that a change in growth form, from cylindrical to polygonal, is a plausible scenario. It is, however, interesting to note that not all junctions between sectors of planar layers in polygonal forms are angular, and a proportion are formed of small, curved sections. As such, the cylindrical core is frequently not the only portion of a prismatic form that shows layer curvature.

Regardless of the origin of these curved *vs* planar arrangements, the internal change in morphology is also likely to be an important factor for understanding the porosity characteristics of HNTs, because many of the nanopores observed in polygonal forms occur at the junction between the inner cylindrical core and the outer polygonal layers. In addition to the study by Dixon & McKee (1974), the slit-like pores that separate the layer packets in prismatic samples have been previously noted in earlier studies of halloysite using TEM methods – for example, by Kohyama *et al.* (1978) and by Churchman *et al.* (1995). In those studies, the presence of pores in the prismatic samples was attributed to layer packing or to the shrinkage of the halloysite layers upon transformation of hydrated (10 Å) halloysite to dehydrated (7 Å) halloysite, which Kohyama *et al.* (1978) observed using an environmental cell. More recently, Berthonneau *et al.* (2015) used TEM on a hydrated and dehydrated spheroidal halloysite to ascertain that the pores were only observed in the dehydrated specimens, supporting the supposition that the pores are formed upon dehydration. Nonetheless, the sizes of several of the pores observed in the samples studied here (e.g. Fig. 6f) suggest that some pores may be formed during growth of the nanotubes, as opposed to solely being attributed to changes upon dehydration. This may be especially relevant for those pores that are situated at the interface between the central cylindrical core and the first polygonal layer packet. A note of caution is warranted, however, as it is difficult to exclude the possibility that some aspects of the internal architecture that is observed for prismatic HNTs may have been mechanically distorted by the microtome process used to obtain the sections and/or due to damage caused by the electron beam in the TEM, although a beam damage origin is thought to be unlikely, as no changes were observed during focusing. Nonetheless, irrespective of whether they have a primary or a secondary origin, such pores will undoubtedly be of some importance for most technological applications of HNTs because the raw halloysite (HNT) materials used in these applications are inevitably materials that have been refined and dried (dehydrated) at various stages and to various degrees during their mining, refining and other industrial processing.

Another important point that is raised by the observed pore structure of HNTs is that in contrast to the central lumen, which should in theory expose an exclusively aluminol surface (excluding any layer edges that may be exposed; Fig. 1), the slit-like pores that characterize prismatic forms must expose both aluminol and siloxane surfaces on opposing sides of the pore 'roof' and pore 'floor', respectively. This may impart a certain polarity in terms of their adsorption properties and thereby have important implications for technological applications that tacitly assume that the central lumen is the only site that exposes the aluminol surface and that the siloxane surface is only exposed on the exterior of the particles. Indeed, it seems probable that the slit-like pores may well have specific characteristics in terms of their adsorption or nano-containment properties compared to the more uniform environment (both in terms of size and surface reactivity) that is expected for the central lumen. Additionally, for applications that require specific pore sizes, use of prismatic forms will undoubtedly present a wider variation in pore size compared to cylindrical forms for which the porosity will be lumen-dominated, although the accessibility of the slit-like pores requires further assessment. The dominant cylindrical *vs* prismatic form of halloysites can be readily determined from X-ray diffraction patterns ('CP index' of Hillier *et al.*, 2016), and this is probably the easiest way to assess individual samples and new deposits of halloysite for industrial applications in relation to dominant nanotube type.

In terms of similarities and differences in the external surface features of the cylindrical and prismatic types of HNTs, these were best revealed by the SEM and particularly the AFM images. In general, edge steps were more difficult to observe on the surface of the smaller cylindrical forms, although it was clear that such steps are omnipresent but smaller in height on cylindrical tubes as compared to those on prismatic forms, where they reached up to 25 nm in height. In both cases, the steps traverse the tubes mainly at acute and obtuse angles. Their orientation with respect to the long axis of the tubes and the crystallographic direction of rolling, as confirmed by Drits *et al.* (2018), suggest, by analogy with plates of kaolinite (e.g. Flegmann *et al.*, 1971), that the edges observed on both types of tubes correspond to the prism faces that may be indexed as (110) and ($\bar{1}$10). The re-entrant angles of the 'saw tooth' arrangements are also indicative of twinning, as is commonly observed in fine particles of kaolinite (Mansfield & Bailey, 1972). Additionally, the layers with the 'saw tooth' edges are seen to extend contiguously around the arrangement of planar sectors; they do not just represent pseudo-hexagonal plates epitaxially arranged on the surface of a planar sector, although complete platy forms with such an appearance are sometimes observed, particularly in SEM images. From the AFM analyses, edge-step sizes were measured across a variety of cylindrical and prismatic samples and ranged from 4.2 to 24.9 nm (Fig. 4). Assuming the layers are dehydrated and therefore close to 0.7 nm in thickness, this represents edges from ~6–35 (1:1 unit) layers in height. This range is similar to the range in the number of layers making up layer packets as observed in the TEM images and presumably indicates a correspondence between the observations from the two microscopies. Both observations suggest growth in tube diameter by a mechanism that effectively adds multiple 1:1 unit layers to the surface of the HNTs. As mentioned earlier, such an assembly of packets of layers was first noted by Dixon & McKee (1974). Furthermore, the

thickening wedge-like arrangements seen in some TEM cross-sections (e.g. Fig. 5e) also suggest that tube growth is likely to proceed *via* a mechanism that continuously adds new layers to the surface. It should also be emphasized that planar edges running parallel to the tube axes (i.e. traversing along the length of the tubes, as in the schematic of Fig. 1) were not observed, and the cartoon illustrations in many publications that show them are inaccurate. Additionally, the ends of the halloysite tubes often terminate in faces normal to the long axis of the tube that, by similar analogy to kaolinite for the 'saw tooth' faces, may be indexed as (010).

Overall, the frequent occurrence of layer edges traversing the external surface of the nanotube and at tube termini, as highlighted by the AFM images for the prismatic nanotubes, are likely to be of some considerable importance for understanding the surface reactivity of HNTs. For instance, Yuan *et al.* (2008) suggested that the morphological details of the surface of HNTs suggested more surface hydroxyl groups than generally supposed. Additionally, Gray-Wannell *et al.* (2020) proposed that prismatic nanotubes displayed a slightly higher phosphate adsorption capacity as compared to cylindrical nanotubes when normalized to surface area, speculating on the presence of proportionally more pH-dependent edge adsorption sites on prismatic forms. Attempts to measure the extent to which steps traverse the surface of one prismatic example indicated a step/edge density of 0.0083 ± 0.0036 m per m^2 of surface. In combination with the typical heights of the steps, this provides some further evidence that the larger prismatic nanotubes are likely to have proportionally more available edge sites compared to the smaller cylindrical forms. In this context, it is also pertinent to note that platy kaolinites also show a well-established trend for the relative proportion of the mean edge surface area to the total surface area to increase with increasing mean particle (plate) thickness (Nadeau, 1985). Presumably, this suggests some further

commonalities in terms of the crystal growth mechanisms of both platy (kaolinite) and tubular (halloysite) kaolin forms.

Finally, it is interesting to note the analogies between prismatic forms of halloysite and so-called Povlen or polygonal serpentines (Cressey & Zussman, 1976; Baronnet & Devouard, 2005) that have been documented for numerous occurrences of the serpentine mineral chrysotile. The latter often display a fivefold axial symmetry, which is suggested also for many of the prismatic halloysites observed in the present study, although prismatic halloysites appear possibly less regular in form. Thus, in the prismatic halloysites, the angles at which the adjacent sides connect is seen to vary considerably, highlighting that they are not uniform in shape. However, a certain degree of caution should be noted regarding these measurements from the cross-sections. Indeed, Berthonneau *et al.* (2015) stressed that since TEM images are projections of the sample, shifts in the alignment of the sample may result in a distorted view of observed angles, which would also apply to measurements of nanotube widths. Kogure *et al.* (2013) also obtained cross-sectional images of prismatic HNTs where four to five major sectors were noted in some prismatic tubes, and one nanotube contained 18 sectors, as verified using selected area electron diffraction. Again, the number of flat faces observed in a minority of AFM images suggests that some of the halloysites examined in the present study may also have multiple sectors in similarity to polygonal serpentines, for which 15 and 30 sectored polygonal forms are commonly observed (Baronnet *et al.*, 1994). Additionally, Baronnet *et al.* (1994) noted that the larger polygonal serpentine fibres are almost always found in the presence of smaller cylindrical fibres, and there is also well-documented evidence of a cylindrical chrysotile core in the interior of many of the polygonal forms (Cressey & Zussman, 1976). This is all suggestive of some further commonality in terms of either growth or transformation
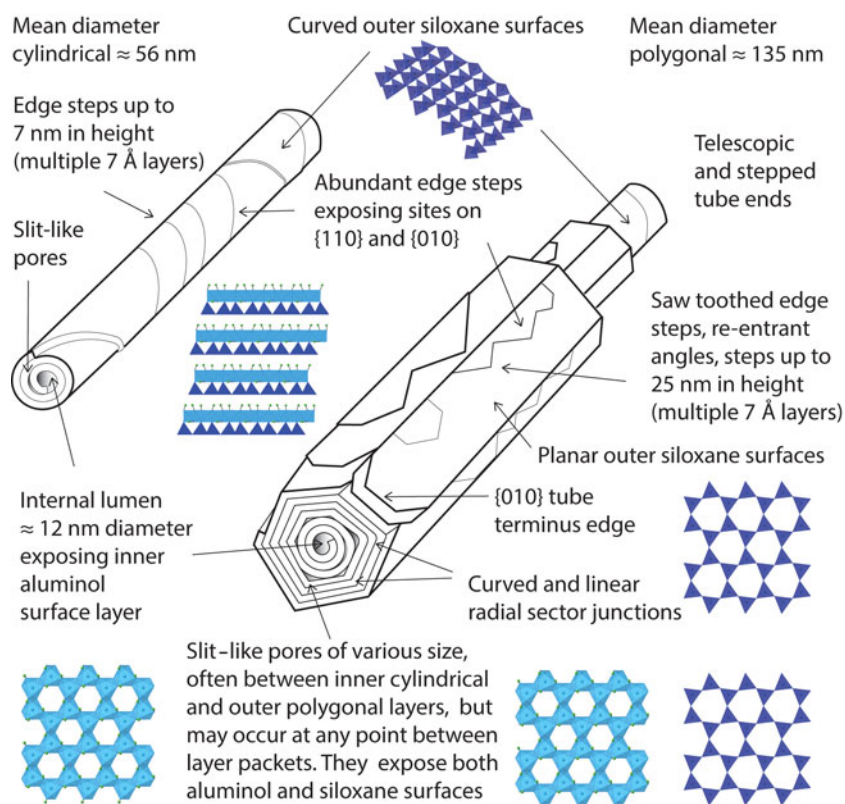

Figure 7. Summary of actual morphological features of HNTs and their surface sites. The layering depicts packets of layers, each packet consisting of multiple 7 Å (1:1) layers (when in largely dehydrated form). Surface sites indicated by octahedral sheet (light blue) and tetrahedral sheet (dark blue) polyhedral models.

mechanisms for the two minerals, notwithstanding that in chrysotile the octahedral sheet is of larger dimensions than the tetrahedral sheet, which is the opposite to that of the kaolins, meaning that the inner and outer surfaces are reversed. It is also interesting to consider that the tendency towards the unusual $2M_1$ polytypic layer stacking sequence that is uniquely observed in some HNTs, particularly those of prismatic form, might in some way be related to periodic changes in hydrogen bonding as a consequence of the spiral rolling of layers in a similar manner to the polytype alternations that have been documented in polygonal serpentines (Baronnet *et al.*, 1994).

Conclusions

The conclusions of the present study in terms of the actual morphological and surface chemistry features of HNTs, as revealed by a combination of SEM, AFM and TEM images collected from nine different samples, are summarized schematically in Fig. 7. Both the smaller, cylindrical and larger, prismatic forms of HNTs have abundant edge sites traversing their outer surfaces. The orientation of the edges indicates that they correspond to the equivalent {110} and {011} kaolinite faces; additionally, the ends of the tubes commonly terminate in the equivalent {010} faces. The intersection of the faces on the tube surface of the larger particles gives a 'saw tooth' appearance indicative of twinning. The heights of the edge steps measured by AFM indicate that they correspond to the packets of tens to several tens of (1:1) layers, as best seen in the TEM cross-sections. The TEM data also revealed that the prismatic forms of halloysite typically have a cylindrical core. This is in good agreement with the interpretation of the powder diffraction patterns of prismatic samples put forward by Drits *et al.* (2018), which requires an integral component with the structural disorder of a cylindrical form. However, the TEM images also show that curved sections of layers can occur at the junction of planar sectors in the more external portions of prismatic samples. For both cylindrical and prismatic forms, the diameter of the central lumen averages ~12 nm. The central lumen with an aluminol surface is the primary nano-confined pore space in cylindrical HNTs, but in prismatic forms additional slit-shaped pores of a wide variety of sizes are present between layer packets, particularly at the interfacial junction between the cylindrical core and the outer planar sectors. These more variably sized pores must also expose both aluminol and siloxane surfaces. However, cross-sections of the long axes of the tubes indicate that, unlike the lumen, the slit-like pores do not extend along the complete length of the tube. The prismatic forms are also likely to have proportionally more edge sites per unit surface, such that, overall, the surface and nanopore properties of prismatic varieties of HNTs are more heterogeneous than HNTs that are predominantly of cylindrical form. Finally, the simple and paramount point we wish to make is that it should be very apparent from the work presented herein that the popularized model of HNTs as a 'carpet roll' nanotube is far too simplistic, and many technological applications that seek to functionalize HNTs might benefit from considering the more realistic model presented herein.

References

Baronnet A. & Devouard B. (2005) Microstructures of common polygonal serpentines from axial HRTEM imaging, electron diffraction, and lattice-simulation data. *Canadian Mineralogist*, **43**, 513–542.

Baronnet A., Mellini M. & Devouard B. (1994) Sectors in polygonal serpentine. A model based on dislocations. *Physics and Chemistry of Minerals*, **21**, 330–343.

Bates T.F. & Comer J.J. (1957) Further observations on the morphology of chrysotile and halloysite. *Clays and Clay Minerals*, **6**, 237–248.

Bates T.F., Hildebrand F.A. & Swineford A. (1950) Morphology and structure of endellite and halloysite. *American Mineralogist*, **35**, 463–484.

Berthonneau J., Grauby O., Jeannin C., Chaudanson D., Joussein E. & Baronnet A. (2015) Native morphology of hydrated spheroidal halloysite observed by environmental transmission electron microscopy. *Clays and Clay Minerals*, **63**, 368–377.

Cavallaro G., Milioto S. & Lazzara G. (2020) Halloysite nanotubes: interfacial properties and applications in cultural heritage. *Langmuir*, **36**, 3677–3389.

Chukhrov F.V. & Zvyagin B.B. (1966) Halloysite, a crystallochemically and mineralogically distinct species. Pp. 11–25 in: *Proceedings of the International Clay Conference Jerusalem, Israel*. Program for Scientific Translation, Jerusalem, Israel.

Churchman G.J., Davy T.J., Aylmore L.A.G., Gilkes R.J. & Self P.G. (1995) Characteristics of fine pores in some halloysites. *Clay Minerals*, **30**, 89–98.

Churchman G.J., Pasbakhsh P. & Hillier S. (2016) The rise and rise of halloysite. *Clay Minerals*, **51**, 303–308.

Cressey B.A. & Zussman J. (1976) Electron microscopic studies of serpentines. *The Canadian Mineralogist*, **14**, 307–313.

Dixon J.B. & McKee T.R. (1974) Internal and external morphology of tubular and spheroidal halloysite particles. *Clays and Clay Minerals*, **22**, 127–137.

Drits V.A., Sakharov B.A. & Hillier S. (2018) Phase and structural features of tubular halloysite (7 Å). *Clay Minerals*, **53**, 691–720.

Du M., Guo B., Lei Y., Liu M. & Jia D. (2008) Carboxylated butadiene–styrene rubber/halloysite nanotube nanocomposites: interfacial interaction and performance. *Polymer*, **49**, 4871–4876.

Flegmann A.W., Love G. & Scott V.D. (1971) Electron-optical study of the prism surfaces of kaolinite microcrystals. *Clay Minerals*, **9**, 245–249.

Gkouma E., Gianni E., Avgoustakis K. & Papoulis D. (2021) Applications of halloysite in tissue engineering. *Applied Clay Science*, **214**, 106291.

Gray-Wannell N., Holliman P.J., Greenwell H.C., Delbos E. & Hillier S. (2020) Adsorption of phosphate by halloysite (7 Å) nanotubes (HNTs). *Clay Minerals*, **55**, 184–193.

Grylewicz A. & Mozia S. (2021) Polymeric mixed-matrix membranes modified with halloysite nanotubes for water and wastewater treatment: a review. *Separation and Purification Technology*, **256**, 117827

Hillier S., Brydson R., Delbos E., Fraser T., Gray N., Pendlowski H. *et al.* (2016) Correlations among the mineralogical and physical properties of halloysite nanotubes (HNTs). *Clay Minerals*, **51**, 325–350.

Joussein E., Petit S., Churchman J., Theng B., Righi D. & Delvaux B. (2005) Halloysite clay minerals – a review. *Clay Minerals*, **40**, 383–426.

Kim T., Kim S., Lee D.K., Seo B. & Lim C.-S. (2017) Surface treatment of halloysite nanotubes with sol–gel reaction for the preparation of epoxy composites. *RSC Advances*, **7**, 47636–47642.

Kogure T., Mori K., Kimura Y. & Takai Y. (2011) Unraveling the stacking structure in tubular halloysite using a new TEM with computer-assisted minimal-dose system. *American Mineralogist*, **96**, 1776–1780.

Kogure T., Mori K., Drits V.A. & Takai Y. (2013) Structure of prismatic halloysite. *American Mineralogist*, **98**, 1008–1016.

Kohyama N., Fukushima K. & Fukami A. (1978) Observation of the hydrated form of tubular halloysite by an electron microscope equipped with an environmental cell. *Clays and Clay Minerals*, **26**, 25–40.

Lin Y., Wang X., Liu J. & Miller J.D. (2017) Natural halloysite nano-clay electrolyte for advanced all-solid-state lithium–sulfur batteries. *Nano Energy*, **31**, 478–485.

Lvov Y., Wang W., Zhang L. & Fakhrullin R. (2016) Halloysite clay nanotubes for loading and sustained release of functional compounds. *Advanced Materials*, **28**, 1227–1250.

Mansfield C.F. & Bailey S.W. (1972) Twin and pseudotwin intergrowths in kaolinite. *American Mineralogist*, **57**, 411–425.

Massaro M., Lazzara G., Milioto S., Noto R. & Riela S. (2017) Covalently modified halloysite clay nanotubes: synthesis, properties, biological and medical applications. *Journal of Materials Chemistry B*, **5**, 2867–2882.

Nadeau P.H. (1985) The physical dimensions of fundamental clay particles. *Clay Minerals*, **20**, 499–514.

Pasbakhsh P., Churchman G.J. & Keeling J.L. (2013) Characterisation of properties of various halloysites relevant to their use as nanotubes and microfibre fillers. *Applied Clay Science*, **74**, 47–57.

Rueden C.T., Schindelin J., Hiner M.C., DeZonia B.E., Walter A.E., Arena E.T. & Eliceiri K.W. (2017) *ImageJ*2: *ImageJ* for the next generation of scientific image data. *BMC Bioinformatics*, **18**, 529.

Santagata M. & Johnston C.T. (2022) A study of nanoconfined water in halloysite. *Applied Clay Science*, **221**, 106467.

Yuan P., Southon P.D., Liu Z., Green M.E.R., Hook J.M., Antill S.J. & Kepert C.J. (2008) Functionalization of halloysite clay nanotubes by grafting with γ-aminopropyltriethoxysilane. *The Journal of Physical Chemistry C*, **112**, 15742–15751.

Yuan P., Tan D. & Annabi-Bergaya F. (2015) Properties and applications of halloysite nanotubes: recent research advances and future prospects. *Applied Clay Science*, **112–113**, 75–93.